



Prediction of interfaces of geological formations using the multivariate adaptive regression spline method

Xiaohui Qi^a, Hao Wang^a, Xiaohua Pan^a, Jian Chu^{a,*}, Kiefer Chiam^b

^a School of Civil and Environmental Engineering, Nanyang Technological University, 639798, Singapore

^b Building and Construction Authority, 200 Braddell Road, 579700, Singapore

Received 19 January 2020; received in revised form 15 February 2020; accepted 15 February 2020

Available online 19 March 2020

Abstract

The design and construction of underground structures are significantly affected by the distribution of geological formations. Prediction of the geological interfaces using limited data has been a difficult task. A multivariate adaptive regression spline (MARS) method capable of modeling nonlinearities automatically was used in this study to spatially predict the elevations of geological interfaces. Borehole data from two sites in Singapore were used to evaluate the capability of the MARS method for predicting geological interfaces. By comparing the predicted values with the borehole data, it is shown that the MARS method has a mean of root mean square error of 4.4 m for the predicted elevations of the Kallang Formation–Old Alluvium interface. In addition, the MARS method is able to produce reasonable prediction intervals in the sense that the percentage of testing data covered by 95% prediction intervals was close to the associated confidence level, 95%. More importantly, the prediction interval evaluated by the MARS method had a non-constant width that appropriately reflected the data density and geological complexity.

Keywords: Geological interface; Rockhead; Multivariate adaptive regression spline; Spatial prediction

1 Introduction

Geological uncertainty plays a crucial role in geotechnical engineering because rational geotechnical design requires a reliable soil profile, geologic profile, or location of rockhead. Increasing efforts have been devoted to predicting the boundaries of soil layers (e.g., Cao & Wang, 2012; Ching, Wang, Juang, & Ku, 2015), the distribution of soil layers (e.g., Qi, Li, Phoon, Cao, & Tang, 2016; Li, Qi, Cao, Tang, Phoon, & Zhou, 2016; Deng, Li, Qi, Cao, & Phoon, 2017; Wang, Wang, Liang, Zhu, & Di, 2018; Li, Cai, Li, & Zhang, 2019), and the interface of different geological formations or the interface of soil and rock (e.g., Dasaka & Zhang, 2012; Priya & Dodagoudar, 2015; Wang, Wellmann, Li, Wang, & Liang, 2017). The prediction should provide a mean value and a standard deviation

or a standard error of the predicted value for an unknown parameter as the latter is an important index reflecting the confidence level of prediction.

A well-known challenge of the spatial prediction problem is limited data. The problem is quite severe for the interpolation of rockhead or interface of geological formations as one drilled borehole or subsurface sounding provides at most one measurement for a specific geological interface. As a result, geostatistical methods such as the kriging, the conditional random field method (e.g., Qi & Liu, 2019), and the multiple-point geostatistics may not be effective because the available data are not sufficient for spatial variability characterizations. The coupled Markov chain method has been demonstrated by Qi, Li, Phoon, Cao, & Tang (2016) and Li, Cai, Li, & Zhang (2019) to perform well when limited data are available. However, it can only be applied to cases where different soil or geological layers are embedded into each other and the soil or geological layer sequence possesses a Markovian property. The Markov random field method (e.g., Wang, Wellmann, Li, Wang, & Liang, 2017) is able to model

* Corresponding author.

E-mail addresses: qixiaohui@ntu.edu.sg (X. Qi), wang.hao@ntu.edu.sg (H. Wang), xhpan@ntu.edu.sg (X. Pan), cjchu@ntu.edu.sg (J. Chu), Kiefer_CHIAM@bca.gov.sg (K. Chiam).

complex geological structures and simultaneously quantify the geological and geotechnical uncertainty. However, the model specifications of the Markov random field method are not clear as described by Mariethoz and Caers (2014). Recently, Wang and Zhao (2016, 2017), Wang, Akeju, & Zhao (2017), Zhao, Hu, & Wang (2018), Zhao, Montoya-Noguera, Phoon, & Wang (2018) developed a Bayesian compressive sampling method that treated geotechnical data as samples of a signal. By approximating the signal with a weighted sum of some basis functions such as cosine functions, the spatial interpolation task was transformed into a task of determining the suitable weights of the basis functions. This method was shown by Wang, Akeju, & Zhao (2017) to have a higher accuracy than other well-known spatial interpolation methods such as cubic spline, polynomial regression, and the ordinary kriging method. One potential problem of the Bayesian compressive sampling method is that the shape of the resulting signal or soil/geological profile depends highly on the adopted basis functions, such as a wavy shape for cosine basis functions. In addition, it does not deal with the issue of heteroscedasticity. Therefore, it was not used in the estimation of the surface of geological interfaces, for which the shape is rather complex and chiefly dominated by geological environments and major geological structures such as faults and folds. In contrast, another spatial prediction method, namely the spline regression method, automatically captures the nonlinearities and complex trends of geological interfaces. Qi, Pan, Chiam, Lim, and Lau (2020) illustrated that the one-dimensional spline regression method performed well with limited one-dimensional rockhead data. In addition, the method provided a reasonable standard deviation of a prediction and differentiated zones with different prediction uncertainties.

Therefore, this study continues to explore the capabilities of the spline regression method in dealing with 2D geological data. A multivariate spline regression method called multivariate adaptive regression spline (MARS) was used to spatially predict the surface of geological interfaces. The MARS method is different from the one-dimensional spline regression tool used by Qi, Pan, Chiam, Lim, & Lau (2020) that dealt only with one-dimensional problem. The MARS method is well known for its ability to automatically model nonlinearities and interactions among different factors (Friedman, 1991; Hastie, Tibshirani, & Friedman, 2008). It has been applied to the geotechnical engineering such as reliability analyses of geotechnical structures (e.g., Zhang & Goh, 2017; Liu, Zhang, Cheng, & Liang, 2019), lateral wall deflection estimation (e.g., Zhang, Zhang, & Goh, 2018; Zhang, Zhang, Wang, Zhang, & Goh, 2019; Zhang, Zhang, Wu, Goh, Lacasse, Liu, & Liu, 2019), rock-depth predictions (Samui, Kim, & Viswanathan, 2015), and other geotechnical problems (e.g., Zhang & Goh, 2013; Zhang et al., 2015, 2017; Goh, Zhang, Zhang, Zhang, & Xiao, 2017). However, to the best of our knowledge, few studies have considered prediction uncertainties or fitting errors. In this study, borehole data

from two sites in Singapore were used to illustrate the spatial predictions. The two sets of borehole data reveal the interface of the Kallang Formation (KF) and Old Alluvium (OA) (two deposit formations) and the rockhead of Bukit Timah Granite (BTG) (an igneous rock formation), respectively. The location of both types of interface is vital information for construction work because both separate relatively strong materials from relatively soft materials. The performance of the MARS method was evaluated using a cross-validation procedure.

2 Method

The MARS method is a well-known nonparametric regression technique. It can model nonlinear patterns without knowing the exact form of nonlinearities prior to model training. Since its advent in 1991 (Friedman, 1991), the method has been widely used in various areas such as hydrology (e.g., Kisi & Parmar, 2016) and transportation (e.g., Chang, 2017). It has also found wide applications in geotechnical engineering such as in slope stability analyses by Samui (2012) and Wang, Wu, Gu, Liu, Mei, & Zhang (2020), tunnel problems by Adoko, Jiao, Wu, Wang, and Wang (2013), Goh, Zhang, Zhang, Xiao, and Xiang (2018), and Zhang, Li, Wu, Li, Liu, & Liu (2020), and pile drivability predictions by Zhang and Goh (2016) and Zhang, Wu, Li, Wang, & Samui (2019).

The core of the MARS method is the spline, a continuous piecewise polynomial function. The MARS model is expressed by a weighted average of basis functions, $B_i(x)$, given as

$$f(x) = \sum_{i=1}^N c_i B_i(x), \quad (1)$$

where N is the total number of terms in the function, c_i is a constant coefficient estimated by the least squares method, and x is an independent parameter (also called a predictor, such as a horizontal coordinate in the spatial prediction problem investigated herein). The basis function is a series of polynomial functions where the order is specified by the user. For example, if a linear spline is used, the basis function can only take the following three forms: (i) a constant 1, (ii) a hinge function or (iii) a product of two or more hinge functions for different predictors. A hinge function is given by

$$\max(x - t, 0) \text{ or } \max(t - x, 0), \quad (2)$$

where $\max(\cdot, \cdot)$ denotes the maximum of two given values and t is the knot, namely the location where two neighboring polynomial pieces meet. The MARS method can be viewed as a generalization of the piecewise polynomial regression. The basic idea of the MARS method is to capture the nonlinear relationship between predictors and dependent parameters (also called responses) by determining suitable knots and basis functions. The MARS procedure consists of two steps. In step 1, knots and basis functions are gradually added to the current model to minimize fitting errors (e.g., the sum of squared errors). The

knot is selected from a set of candidate knots assumed to be located at the predictor values of observations. For example, consider a case with N_o observations of the geological interface and with two predictors for each observation, namely the coordinates x and y . If all the observations have different coordinates, the number of candidate knots is equal to the number of observations \times the number of predictors $= 2 \times N_o$. Suitable knots are gradually added to the MARS model one by one, and in each round of knot addition, the candidate knot that minimizes the fitting error is considered to be the most suitable knot (see [Hastie, Tibshirani, & Friedman, 2008](#) for details). In step 2, the basis functions (or terms in Eq. (1)) that do not contribute significantly to prediction accuracy are removed. Step 2 is known as “pruning” and is implemented because the model obtained from step 1 includes many knots and fits well to the training data but may not be well generalized to the new data. To prune a model, the suitable number of terms to be retained must be known. Two methods commonly used to determine the optimal number of terms are the generalized cross-validation index (GCV) and k -fold cross-validation. The GCV index is an estimator of the mean squared error of predictions and considers the fitting capacity and the complexity of candidate models ([Friedman, 1991](#); [Hastie, Tibshirani, & Friedman, 2008](#)). k -fold cross-validation is a process that randomly splits a dataset into k groups or folds of approximately equal size and trains

and validates the model by setting $k - 1$ folds of data as training data and the remaining one fold as validation data ([James, Witten, Hastie, & Tibshirani, 2013](#)). In each round of cross-validation, various numbers of terms are used, and each number leads to a mean squared error for the validation data (e.g., $MSE_{1,t}$ is the mean squared error for t terms when fold 1 is used for validation). This cross-validation is repeated k times by sequentially setting one fold of data as the validation data. The k rounds of cross-validation produce k mean squared errors for each number of terms (e.g., t terms corresponding to $MSE_{1,t}$, $MSE_{2,t}$, ..., $MSE_{k,t}$). The optimal number of terms in the MARS model is that producing the minimum average value of the k mean squared errors. The procedure of the k -fold cross-validation is plotted in [Fig. 1](#). To further improve the robustness of the model, the k -fold cross-validation is repeated N_{cross} times, each of which performs a new splitting of the data ([Milborrow, 2019a, 2019b](#)). After the optimal number of terms has been determined, the MARS model is built using all the k folds of data and the optimal number of terms. Details of the MARS method can be seen in [Friedman \(1991\)](#), [Hastie, Tibshirani, & Friedman \(2008\)](#), and [Zhang and Goh \(2016\)](#). The MARS method is incorporated in the software packages of “earth” in the R platform and the ARESLab toolbox of MATLAB (downloadable at <http://www.cs.rtu.lv/jekabsons/regression.html>). The main difference between the two tools is that the former uses only

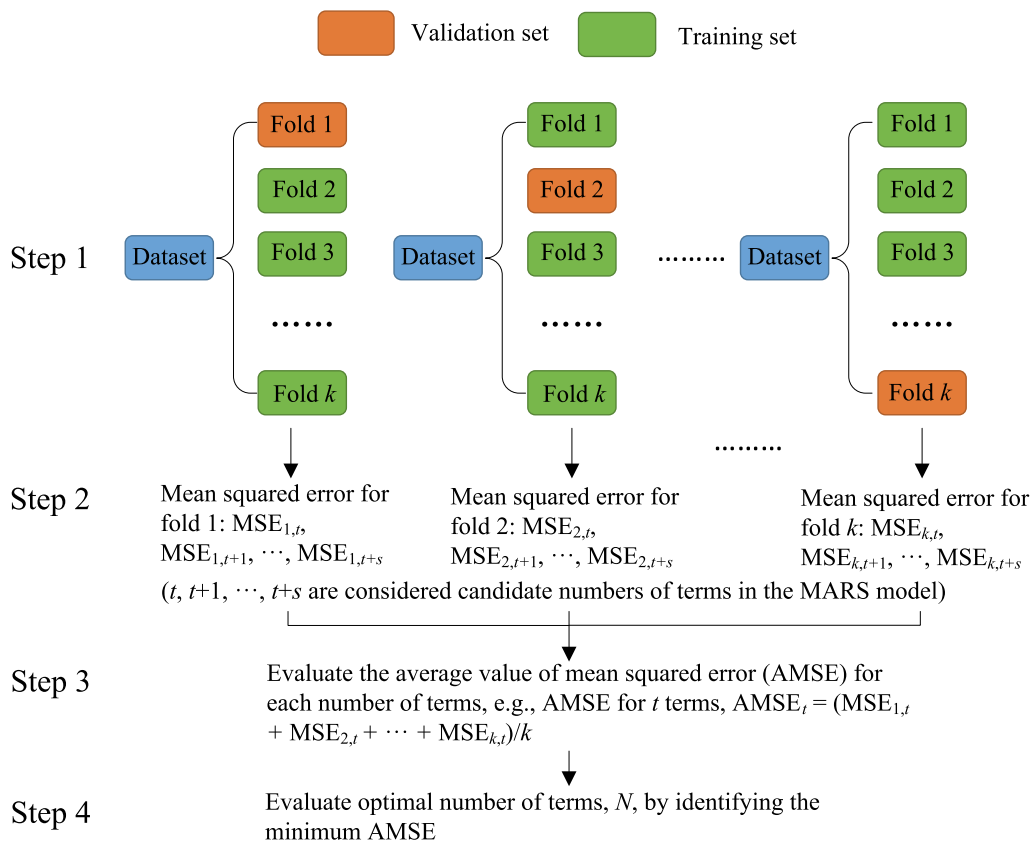


Fig. 1. The procedure of k -fold cross-validation for building the multivariate adaptive regression spline model.

linear splines and is able to consider prediction uncertainties, while the latter uses linear and cubic splines but cannot consider prediction uncertainty. In this study, the “earth” package was used because prediction uncertainty is one of the major concerns in the spatial predictions of geological interface locations.

It is worth noting that the “earth” package in the R platform contains variance models that can be used to evaluate the prediction interval of a response. These variance models are not components of the MARS method but have been developed independently by other researchers (e.g., Davidian & Carroll, 1987; Carroll & Ruppert, 1988; Gałeczki & Burzykowski, 2013). One notable feature of these variance models is that heteroscedastic errors (or residuals) can be considered, thereby leading to a non-constant prediction interval. The basic principle of the variance model is to divide the variance of the prediction error into two parts; namely, model variance and noise variance. The former is a measure of how the model varies across training samples (different training samples resulting in different knots and basis functions), while the noise variance reflects how far the actual values of training samples deviate from the fitted values (or the mean trend) in one regression. The model variance is evaluated by computing the variance of predicted values for the validation data in N_{cross} cross-validations (Milborrow, 2019a, 2019b), where N_{cross} is the time of repetition of the k -fold cross-validation. To be specific, the prediction interval is obtained by the following procedure.

- (i) Construct a regression model that relates the absolute error of the MARS model (output) with the predictors or the predicted value of the MARS model (input). In this study, the predictors, namely the two horizontal coordinates x and y , are considered to be the input of the regression model. The output of the regression model, namely the absolute error of the MARS model, is the absolute error for a future prediction. It is estimated from the raw residual of the MARS model and the model variance as (e.g., Milborrow, 2019b)

$$E^2 = \frac{R^2}{1-h} + V_m, \quad (3)$$

where E^2 is the squared prediction error, R^2 is the squared raw residual, and V_m is the estimated model variance at a point. The raw residual is the difference between the observed value and fitted value for an observation used for regression, and h is one point's leverage that is a measure of how far away the independent value of an observation is from those of other observations. An observation with a large leverage has a large influence on the regression (e.g., Milborrow, 2019b). The regression model can take any linear or nonlinear form such as an exponential function, or another spline function.

- (ii) Assuming normality, rescale the absolute error to an estimated standard deviation, $\hat{\sigma}$ using (e.g., Milborrow, 2019b)

$$\hat{\sigma} = 1.25 \times \mu_{|E|}, \quad (4)$$

where $\mu_{|E|}$ is the mean of absolute error.

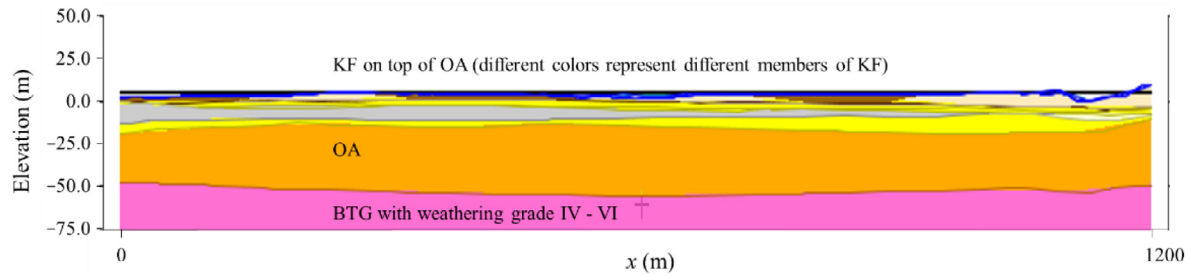
- (iii) Convert the standard deviation to a prediction interval, PI, for a given confidence level, $1 - \alpha$, as

$$\text{PI} = \hat{\mu} \pm z_{\alpha/2} \times \hat{\sigma}, \quad (5)$$

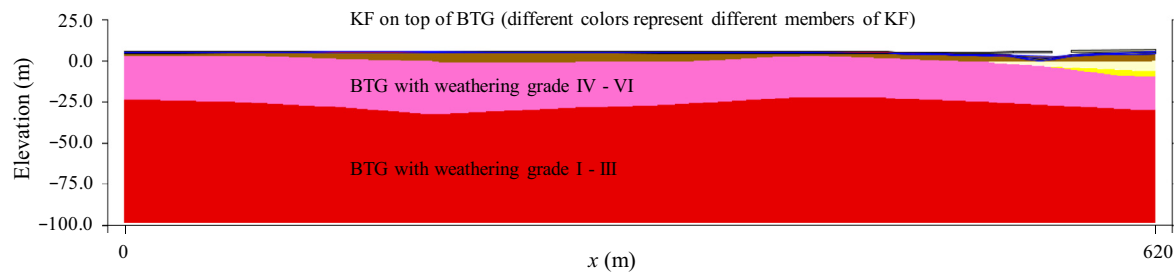
where $\hat{\mu}$ is the predicted mean value, $z_{\alpha/2}$ is the quantile associated with a cumulative probability $1 - \alpha/2$. For example, as $\alpha = 0.05$, the prediction interval associated with a 95% confidence level is $\hat{\mu} \pm 1.96 \times \hat{\sigma}$. Herein, the underlying assumption was that the considered parameter had a normal distribution. More information about the variance model can be found in the manual of the “earth” package or Milborrow (2019a, 2019b).

3 Borehole data

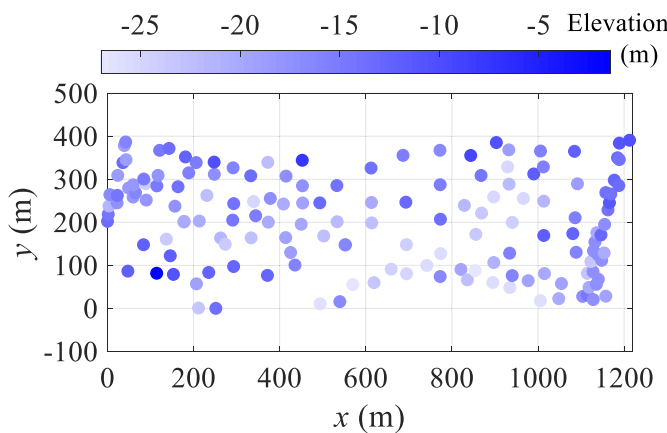
The borehole data collected from two sites in Singapore were used to illustrate the application of the MARS method. The first site was at Upper Changi Road, Tampines, and the second at Canberra Link, Sembawang, Singapore. The geological profiles of the cross-sections at the two sites are shown in Figs. 2(a) and (b), respectively. The geological profiles were extracted from a 3D geological model constructed by geologists using Subsurface Viewer, a 3D geological modeling software developed by the British Geological Survey (e.g., Aswar & Ullagaddi, 2017; Burke, Ford, Hughes, Thorpe, & Lee, 2017). As shown, the two sites mainly involved KF, OA, and BTG. OA and KF are deposit formations with ages from probably Plio-Pleistocene and late Pleistocene to present, respectively (Pitts, 1984; Sharma, Chu, & Zhao, 1999). The former consists mainly of dense and cemented muddy sand or gravel with lenses of silt and/or clay, while the latter is composed of sediments with marine, alluvial, littoral, and estuarine origins (Pitts, 1984). The OA generally has good geotechnical properties and is one of the major sources of sand used for construction (Sharma, Chu, & Zhao, 1999). On the contrary, the KF is made up of soft or weak sediments and represents a problematic construction material. The BTG is an igneous rock formation developed from the early to middle Triassic period. It underlies approximately one-third of Singapore Island and is recognized as the base rock of Singapore. The top section of the BTG rock has been completely weathered into soil because of the intensive weathering in tropical Singapore. For tunneling constructions, engineers need to know the interface between the KF and the OA for site 1 or the interface between the soil and rock or the so-called rockhead position in



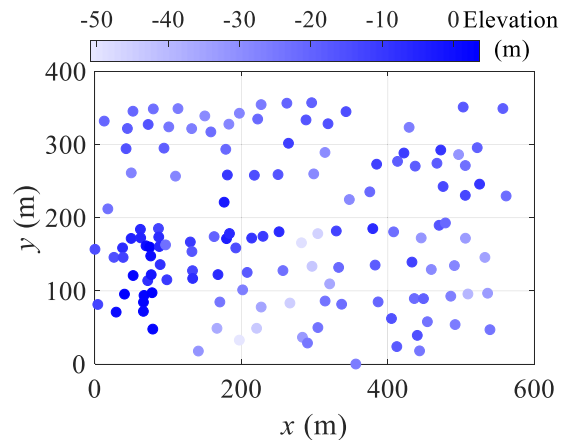
(a) Geological profile of a cross-section at site 1



(b) Geological profile of a cross-section at site 2



(c) Kallang formation–Old Alluvium interface



(d) Bukit Timah granite rockhead

Fig. 2. Geological profiles of cross-sections at two sites and plan view of boreholes.

the BTG for site 2. Numerous factors make the rockhead location highly variable within a short distance. The weathering of BTG in Singapore involves mainly chemical decomposition, which is a complex process affected by a variety of factors including climate, topography, hydrological conditions, biological systems, rock mass discontinuities, rock composition and permeability (Zhao, Broms, Zhou, & Choa, 1994). In addition, the KF–OA interface is affected by variations of river channels and sea level, the topography of the local area, and also has a large variability in underground space. It is a challenging task to predict the KF–OA interface location and the rockhead location in areas between boreholes.

In the engineering practice of Singapore, rockhead is normally viewed to be the interface of the three high weathering grades including moderately weathered, slightly weathered, and fresh, and the three low weathering grades including residual soil, completely weathered rock, and highly weathered rock (e.g., Shirlaw, Hencher, & Zhao, 2000). Rock masses with the former three weathering grades are considered to be rock while those with the latter three grades are considered to be soil. The weathering grade of rock mass in Singapore is determined according to a British code (British Standard Committee, 1999). In a few cases, a thin layer (e.g., thickness <2 m) described as moderately weathered rock, slightly weathered rock, or

fresh rock overlies one of the three types of soil layers. This thin layer is likely to be a boulder and was not considered to be a rock layer in this study. In addition, the weathering grade information of the BTG and interface information of the KF–OA were read directly from borehole logs in site investigation reports.

The plan views of boreholes at the two sites are shown in Figs. 2(c) and (d). In both figures, borehole markers in dark blue denote relatively high elevations of the KF–OA interface or BTG rockhead, while those in light blue denote relatively low elevations. As shown, 154 and 135 boreholes were distributed in an area of 1200 m × 400 m and 550 m × 350 m, respectively. The elevation of the KF–OA interface ranged from −27.0 m to −1.4 m, while the elevation of the BTG rockhead ranged from −50.8 m to 3.6 m. In this study, the elevation was the height relative to the Singapore Height Datum, namely the mean sea level determined by the tide gauge at Victoria Dock from 1935 to 1937. The elevation rather than depth of the geological interface was used because the ground surface is not flat and the depth value is affected by excavation activities while the elevation is not. The elevations of the geological interfaces are summarized in Tables A1 and A2 in the appendix. The mean and standard deviation of the KF–OA interface elevation were −17.7 m and 4.6 m, respectively, while the mean and standard deviation of the BTG rockhead elevation was −18.5 m and 11.6 m, respectively. The rockhead elevation had a significantly larger variability than that of the KF–OA interface elevation. This phenomenon is expected since the BTG has experienced more geological events (volcanic activity and faulting) than the other two formations. For example, Woon and Zhou (2009) stated that little faulting occurred during the main deposition period of the OA.

4 Spatial prediction of geological interface elevations

A spatial prediction of the KF–OA interface elevation and BTG rockhead elevation was conducted using the MARS method. The prediction accuracy was evaluated by a cross-validation procedure. Note that the cross-validation mentioned herein was different from the k -fold cross-validation introduced in Section 2. The k -fold cross-validation was used to build the MARS model, while the cross-validation mentioned herein was used to evaluate the performance of the built model. In the cross-validation of this section, a certain percentage of borehole data were withheld as testing data (the term “testing data” is used to differentiate from the term “validation data” appearing in the k -fold cross-validations), while the remaining data were viewed as training data. The training data were further divided into k folds in k -fold cross-validations to construct the MARS model. The one-fold validation data were used to prune the MARS model (i.e., determine the optimal number of terms), while the testing data were used to assess the prediction accuracy of the built model.

4.1 KF–OA interface

4.1.1 Predicted KF–OA surface using all data

The surfaces of the KF–OA interface were predicted using all the data to gain an understanding of the general trend of the KF–OA interface in the investigated area. For the MARS method, the pruning method was set as a 10-fold cross-validation rather than the GCV method because the latter cannot provide any information involving the model variance used to derive the prediction intervals. The 10-fold cross-validation was repeated 200 times to obtain a robust model. The repetition number of the 10-fold cross-validation was set as 200 to ensure a steady optimal number of terms in the MARS model when different repetition numbers were used. The variance model was set as “x.lm”, which means the standard deviation of the prediction was a linear function of the predictors (coordinates x and y). The cross-validations cost less than 5 minutes on a desktop computer with 16-GB random-access memory and two Intel Core i7 CPUs clocked at 3.4 GHz. The resulting functions for the mean trend of the KF–OA interface, $f(x, y)$ and the standard deviation of prediction are given by

$$\begin{aligned} f(x, y) = & -19.3 + 1.20 \times 10^{-3} \times \max(0, 934.13 - x) \\ & + 1.75 \times 10^{-2} \times \max(0, x - 934.13) \\ & - 2.53 \times 10^{-2} \times \max(0, 262.54 - y) \\ & + 3.71 \times 10^{-2} \times \max(0, y - 262.54) \\ & + 1.09 \times 10^{-4} \times \max(0, 619.17 - x) \\ & \times \max(0, 262.54 - y) + 2.82 \times 10^{-5} \\ & \times \max(0, x - 619.17) \\ & \times \max(0, 262.54 - y) \end{aligned} \quad (6a)$$

Standard deviation of prediction

$$= 5.27 - 5.50 \times 10^{-4} \times x - 3.29 \times 10^{-3} \times y \quad (6b)$$

As shown in Eq. (6a), the MARS model contained three knots located at $x = 619.17$ m, $x = 934.13$ m, and $y = 262.54$ m. The standard deviation of the prediction linearly decreased with an increase in x and y , perhaps because the right-hand side of the region had slightly denser boreholes than the left-hand side, and the upper side had slightly denser boreholes than the lower side. Based on these functions, the regressed value of the KF–OA interface elevation at the borehole sites, the predicted surface of the KF–OA interface, and the 95% prediction intervals of the KF–OA interface elevation for the cross-section of $y = 200$ m are plotted in Figs. 3(a), (b), and (c), respectively. In Fig. 3(c), the 95% prediction interval was evaluated as the interval with upper and lower limits set to be the mean value ± 1.96 times the prediction standard deviation. The 95% prediction interval of the geological interface elevation was evaluated by assuming the geological interface elevation was a normally distributed random variable

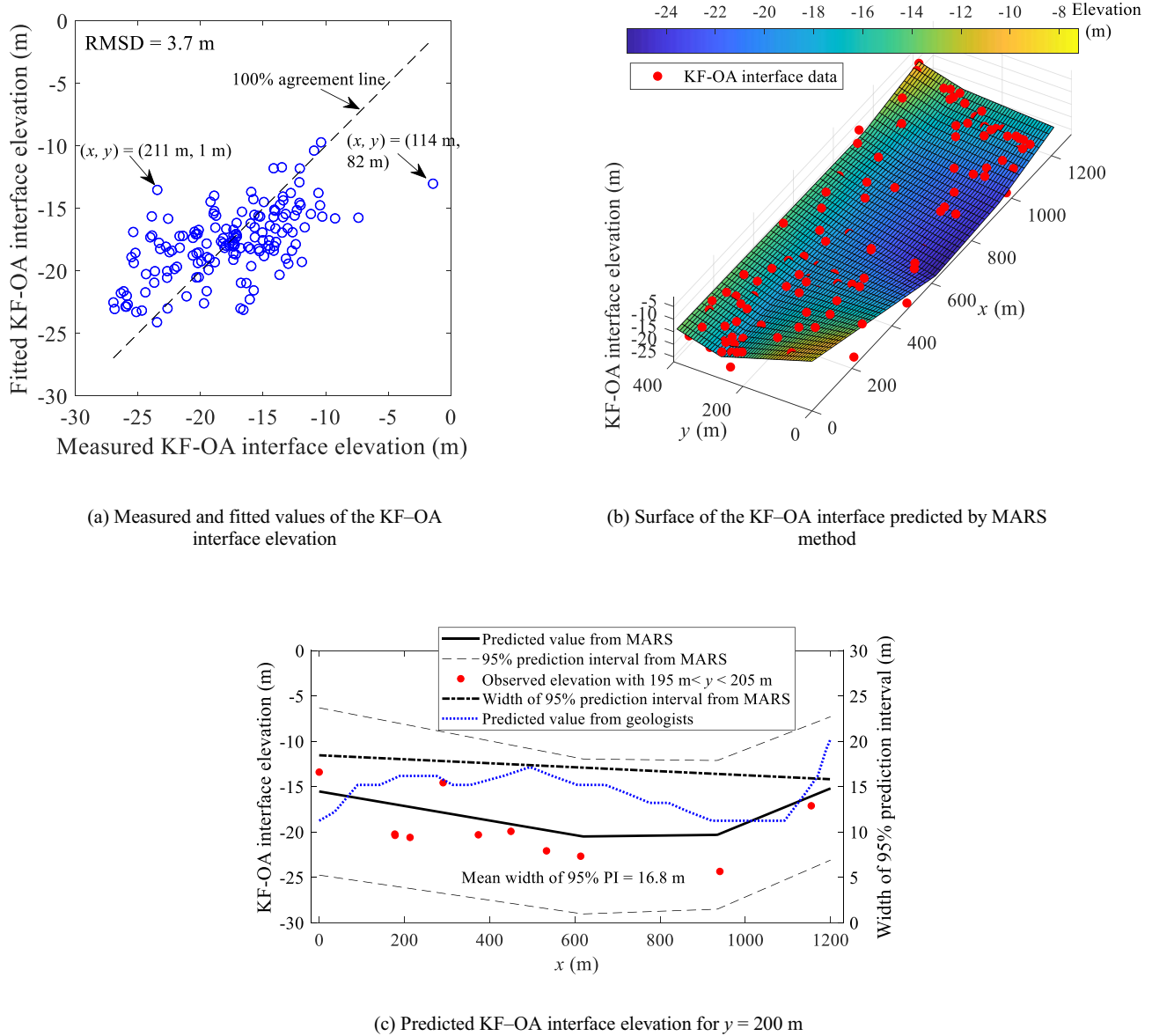


Fig. 3. KF–OA interface elevation predicted by multivariate adaptive regression spline method.

for which the 2.5% and 97.5% quantiles were the mean value ± 1.96 times the standard deviations. For comparison, the predicted curve of geologists in Fig. 2(a) is also plotted in Fig. 3(c) as a dotted line. As shown in Fig. 3(a), the root mean square deviation (RMSD) of the fitting was 3.7 m. The RMSD is given by

$$\text{RMSD} = \sqrt{\frac{1}{N_f} \sum_{i=1}^{N_f} (E_i - \hat{E}_{f,i})^2}, \quad (7a)$$

where N_f is the number of points used for the curve fitting, E_i is the observed value of the geological interface elevation for the i th borehole, $\hat{E}_{f,i}$ is the fitted value of the geological interface elevation for the i th borehole. In Fig. 3(a), the points with relatively large residuals were caused by erratic geological conditions such as a borehole revealing a high KF–OA interface surrounded by several boreholes revealing a relatively low interface (e.g., the borehole located at

$(x, y) = (114 \text{ m}, 82 \text{ m})$, see Fig. 2(c)). As for the trend of the KF–OA interface, one can clearly see from Fig. 3(b) that the lower-left corner and right-hand side of the investigated area had higher KF–OA interfaces than the other zones. In addition, the curve of the KF–OA interface predicted from the MARS method (solid line in Fig. 3(c)) was more accurate than that of the geologists (see the dotted line in Fig. 3(c)). As shown in Fig. 3(c), the KF–OA interface curve predicted by geologists was much farther from the KF–OA interface revealed by boreholes than that predicted by the MARS method.

4.1.2 Consistency of the MARS method

To evaluate the consistency of the MARS method, different percentages of borehole data were withdrawn from the original 154 data points and used for the spatial predictions of the KF–OA interfaces. The data used for the spatial pre-

diction of the KF–OA interface are referred to as training data, and the remainder as testing data. The withdrawn data are shown in Figs. 4(a)–(c). Forty percent of the data were randomly drawn as training data in Fig. 4(a). The training data in Fig. 4(b) contained the training data in Fig. 4(a) and another randomly drawn 20% data, while the training data in Fig. 4(c) contained the training data in Fig. 4(b) and an additional randomly drawn 20% data. The predicted surfaces of the KF–OA interface for the training data in Figs. 4(a)–(c) are plotted in Figs. 4(d)–(f), respectively. As shown in Figs. 4(d)–(f) and Fig. 3(b), when the borehole data were added to the training group and used for spatial predictions, the predicted surface gradually converged to the final surface. In particular, the predicted surface for 80% data was very similar to that for all the data. Furthermore, the predicted KF–OA interfaces along the line $y = 200$ m produced from the training data in Figs. 4(a)–(c) are plotted in Figs. 4(g)–(i), respectively. As shown in Figs. 4(g)–(i) and Fig. 3(c), the average width of the 95% prediction interval of the KF–OA interface elevation gradually decreased as training data were added. The two cases with 80% and 100% data had very similar KF–OA interface curves and

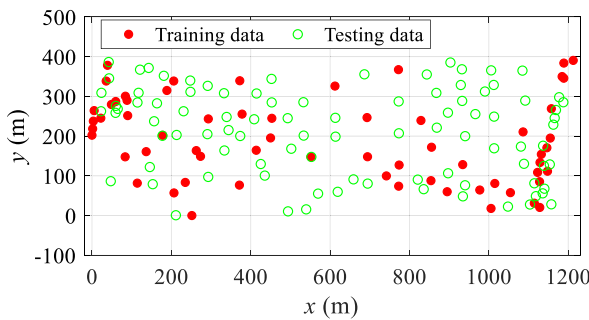
mean widths of 95% prediction intervals (see Fig. 4(i) and Fig. 3(c)), indicating that 123 data points ($80\% \times 154$) may be sufficient to spatially predict the KF–OA interface elevation in this area. In engineering practices, this criterion can be used to determine whether additional boreholes need to be drilled to further reduce the uncertainty of geological interface elevations.

4.1.3 Prediction accuracy of the MARS method

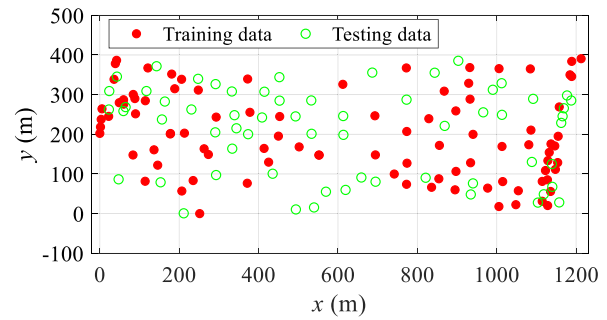
The prediction accuracy of the MARS method was evaluated through a cross-validation method. One hundred cross-validations were performed. 70% of the data were randomly drawn in each trial as training data, and the remaining 30% was used as testing data. The accuracy was denoted by two indexes, namely, root mean square error, RMSE, and root mean square relative error, RMSRE, given by

$$\text{RMSE} = \sqrt{\frac{1}{N_p} \sum_{i=1}^{N_p} (E_i - \hat{E}_i)^2}, \quad (7b)$$

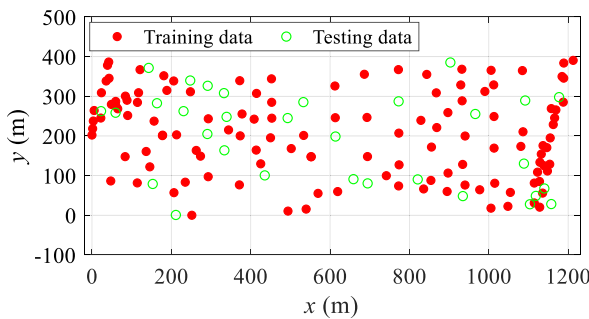
$$\text{RMSRE} = \sqrt{\frac{1}{N_p} \sum_{i=1}^{N_p} \left(\frac{E_i - \hat{E}_i}{D_i} \right)^2}, \quad (7c)$$



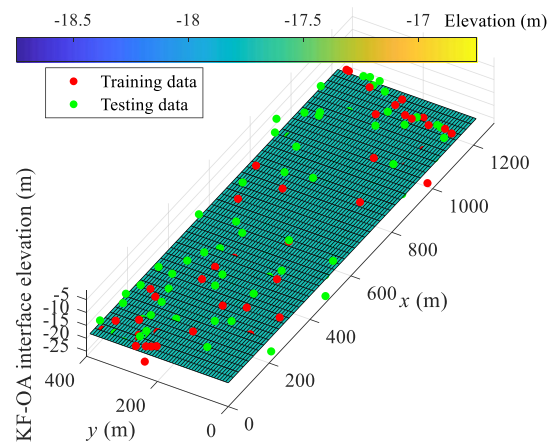
(a) Plan view of borehole data (40% used for prediction)



(b) Plan view of borehole data (60% used for prediction)

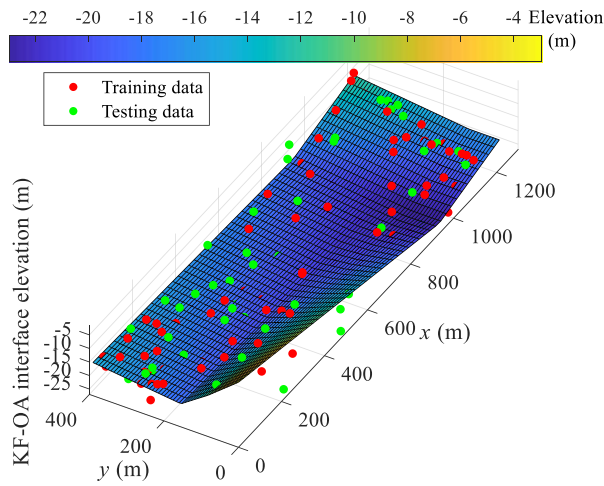


(c) Plan view of borehole data (80% used for prediction)

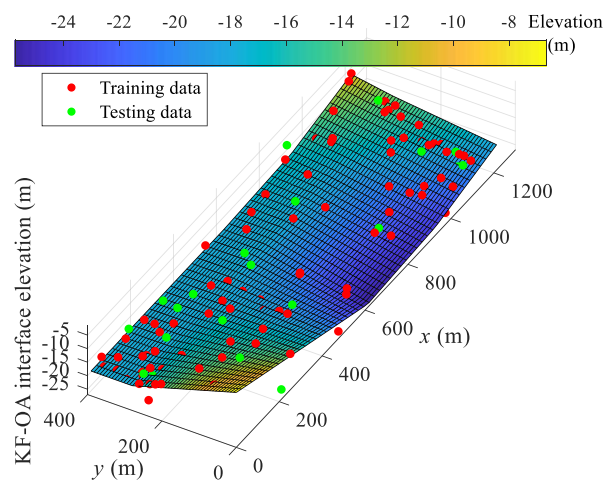


(d) Predicted surface of KF–OA interface (40% data)

Fig. 4. Predicted KF–OA interface elevation using different percentages of data.



(e) Predicted surface of KF–OA interface (60% data)



(f) Predicted surface of KF–OA interface (80% data)

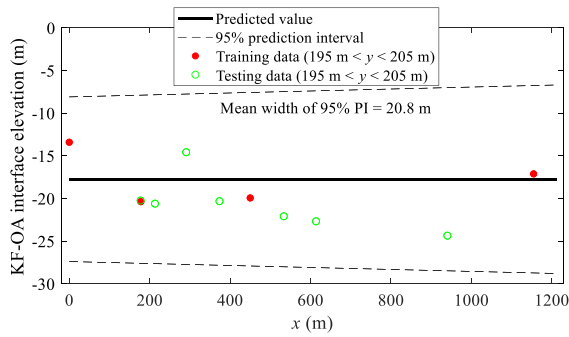
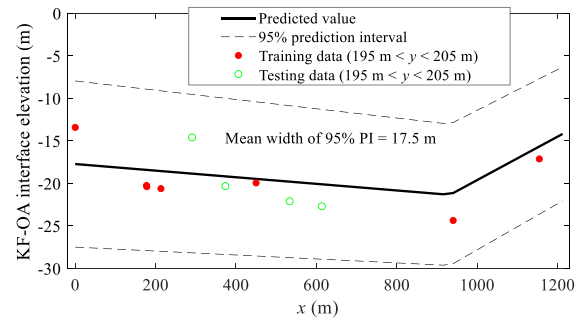
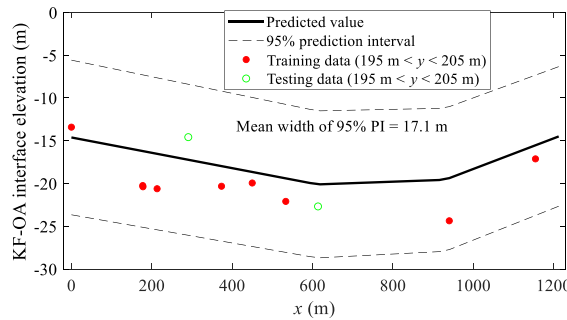
(g) Prediction along $y = 200$ m (40% data)(h) Prediction along $y = 200$ m (60% data)(i) Prediction along $y = 200$ m (80% data)

Fig 4. (continued)

where N_p is the number of points in the testing group, E_i is the observed value of the geological interface elevation for the i th testing borehole, \hat{E}_i is the predicted value of the geological interface elevation for the i th testing borehole, and D_i is the depth of the geological interface at the i th testing borehole. Depth rather than elevation was used in the denominator of Eq. (7c) because sometimes the observed elevation of the geological interface is close to zero. The prediction accuracies for the KF–

OA interface elevation are summarized in Table 1. For brevity, Table 1 lists only the results for 30 experiments. The coverage percentages of the 95% prediction intervals for the MARS method are also summarized in Table 1 because the MARS method can quantify the uncertainty of predictions and provide a prediction interval. The coverage percentage is the percentage of observed values of the KF–OA interface elevation for the testing boreholes covered by the prediction interval. For illustration pur-

Table 1
Prediction accuracies of spatial prediction of KF–OA interface elevation.

Experiment	RMSE (m)	RMSRE	CP (%)
1	5.17	0.61	98
2	4.25	0.19	93
3	3.99	0.17	93
4	4.75	0.20	96
5	5.47	0.59	93
6	5.33	0.61	91
7	4.60	0.50	93
8	4.50	0.21	96
9	4.13	0.24	93
10	4.82	0.55	89
11	3.51	0.20	98
12	4.43	0.23	100
13	4.87	0.23	89
14	4.39	0.40	96
15	4.90	0.56	96
16	4.55	0.23	93
17	4.43	0.46	96
18	4.50	0.46	91
19	3.95	0.20	98
20	4.46	0.21	93
21	3.94	0.43	98
22	3.57	0.17	100
23	4.30	0.21	98
24	3.75	0.19	98
25	4.51	0.40	91
26	4.25	0.20	98
27	5.02	0.56	96
28	3.39	0.18	100
29	4.54	0.47	98
30	4.07	0.20	96
Average	4.40	0.32	95

Note: the last row summarizes the average value for 100 experiments. For brevity, the table only lists the results for 30 experiments.

poses, Figure 5 plots the spatial prediction of the KF–OA interface for Experiment 3 in Table 1, including a plan view of training and testing data, the predicted surface of the KF–OA interface, and the predictions along two cross-sections with $y = 100$ m and 200 m. The following phenomena are observed in Fig. 5 and Table 1.

- (1) The prediction surface of the KF–OA interface of Experiment 3 as shown in Fig. 5(b) generally captured the spatial trend of the interface. As shown in Fig. 5(b) and Fig. 3(b), both surfaces (predicted from 70% data and 100% data, respectively) show that the lower-left and right-hand sections of the area had higher KF–OA interfaces than the other sections. In addition, the lowest KF–OA interface was located around $(x, y) = (800 \text{ m}, 0 \text{ m})$.
- (2) The 95% prediction intervals of the KF–OA interface elevation along the two cross-sections $y = 100$ and 200 m cover the actual values of elevations for the testing data located around the cross-sections (see Figs. 5(c) and (d)). In addition, the prediction intervals had widths consistent with the data density. As shown in Fig. 5(a), the right-hand side of the area, in particular the zone of $1100 \text{ m} < x < 1200 \text{ m}$, was occupied by training data denser than the left-hand

side. In addition, the upper side of the area (i.e., $y > 200 \text{ m}$) also had denser training data than the lower side (i.e., $y < 200 \text{ m}$). Correspondingly, the width of the prediction interval decreased with an increase in the value of x for both cross-sections, and the cross-section of $y = 100 \text{ m}$ had a wider prediction interval than the cross-section of $y = 200 \text{ m}$.

- (3) Since the 95% prediction intervals of the KF–OA interface elevation for both cross-sections covered the actual value of the testing data, one possible concern of readers is whether the prediction interval was too wide or whether the uncertainty of the KF–OA interface elevation in unexplored locations was overestimated. The answer is no as for the considered case, 2 out of 46 testing points cannot be covered by 95% prediction intervals. The coverage percentage ($1 - 2/46 = 95.6\%$) is generally consistent with the confidence level of the prediction interval, 95%. Moreover, the other experiments in Table 1 exhibited similar coverage percentages. As shown in the last row of Table 1, the average value of the coverage for the investigated 100 experiments was the same as that of the confidence level, 95%. This consistency indicates that the MARS method produced a prediction interval that neither overestimated nor underestimated the uncertainty of the geological interface elevations in unexplored areas.
- (4) The mean RMSE of the 100 experiments was only 4.4 m, indicating that the spatial prediction of the KF–OA interface elevation in the investigated area had a relatively low prediction error.

4.2 BTG rockhead

A spatial prediction of the BTG rockhead elevation was performed using the MARS method. Figure 6 plots the predicted rockhead surface and the prediction along the cross-section of $y = 150 \text{ m}$. As shown in Fig. 6(b), the 95% prediction interval of the rockhead elevation was wider in the central and right-hand side than in the other sections. The reason is that the central section had an erratic geological condition and the right-hand side had sparser data than the other sections (see Fig. 2(d)). As shown in Fig. 2(d), the area around $(x, y) = (300 \text{ m}, 150 \text{ m})$ was occupied by several boreholes revealing significantly lower rockhead than the surrounding boreholes. Hence, the prediction interval of the MARS method reflected well the geological regularity and data density.

Fifty cross-validations were performed to evaluate the prediction accuracy of the MARS method. In each round, 70% of the training data were randomly drawn for training, and the remaining 30% were used for testing. The RMSE and RMSRE of the cross-validations for the BTG rockhead are summarized in Table 2. For brevity, only the results for 30 cross-validations are listed. As shown in Table 2, the mean RMSE for the 50 experiments was as

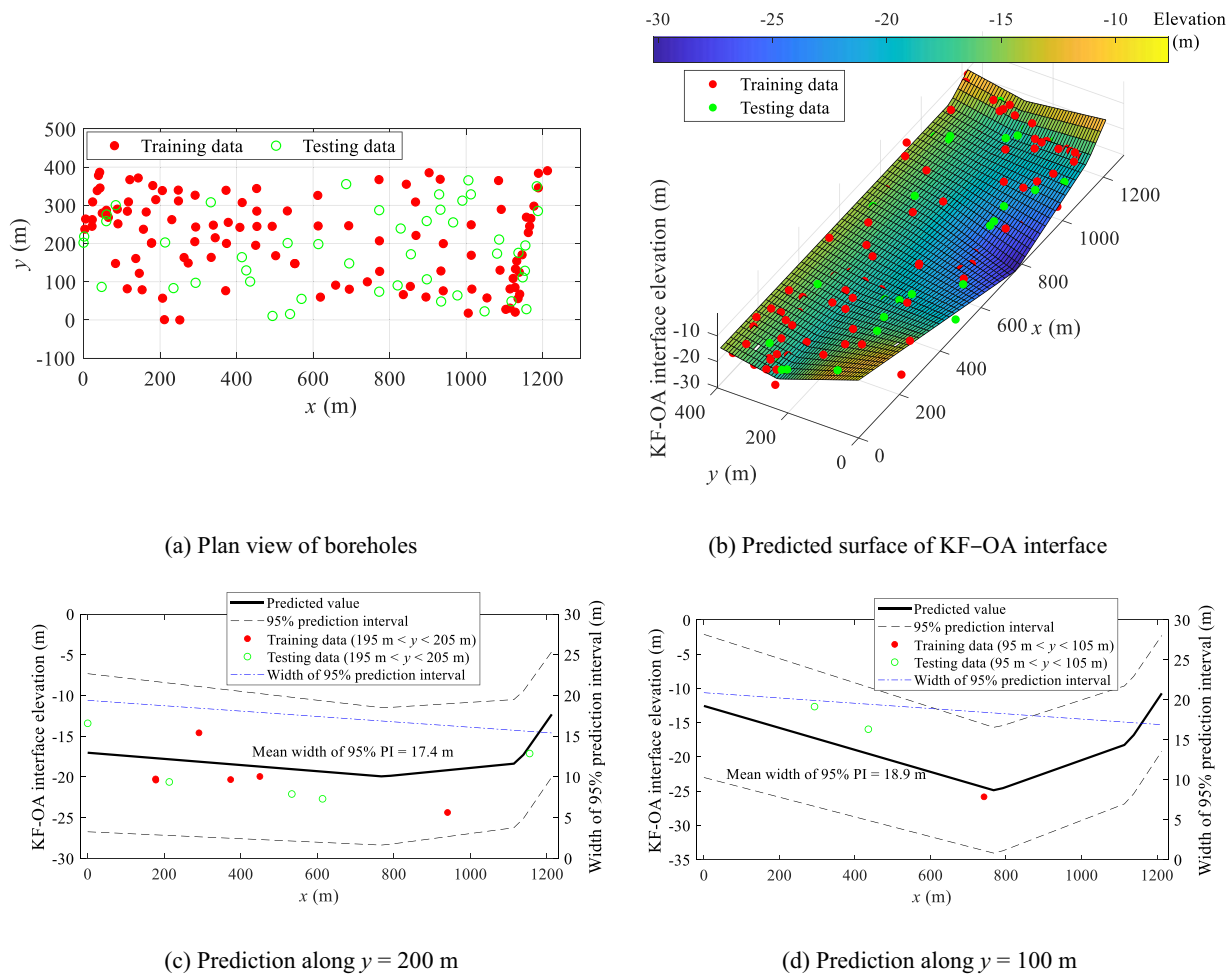


Fig. 5. Cross-validation case of KF–OA interface (Experiment 3 in Table 1).

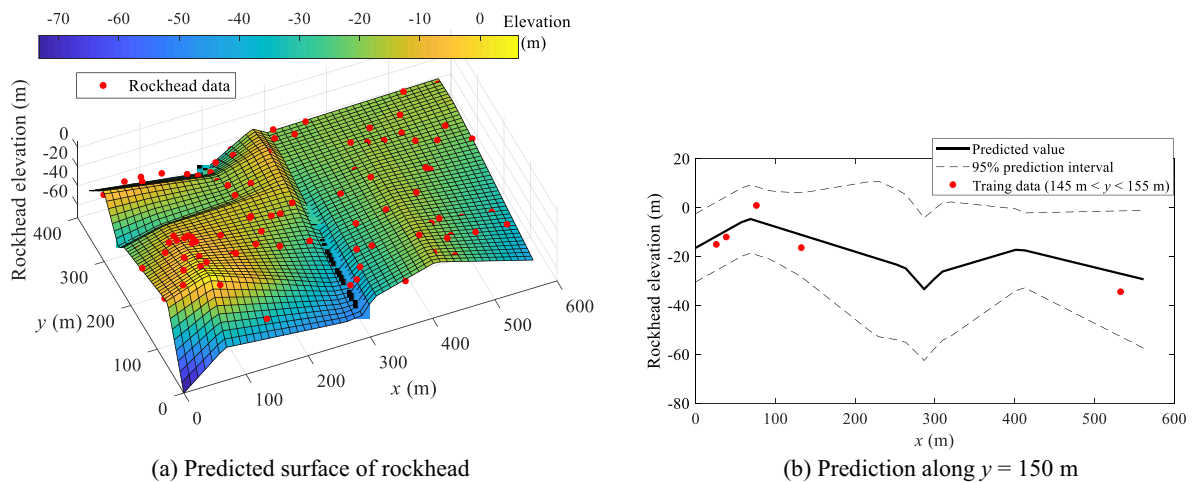


Fig. 6. BTG rockhead elevation predicted by the multivariate adaptive regression spline method.

high as 9.2 m, which was higher than that of the KF–OA interface elevation investigated in Section 4.1. This result was expected because the rockhead elevation had a larger variability than that of the KF–OA interface as discussed in Section 3. Moreover, the average coverage percentage

of the prediction intervals for the BTG rockhead elevation was 98%, which is close to the confidence level, 95%. This result further indicates that the MARS method provided a reasonable prediction interval.

Table 2
Prediction accuracies of spatial prediction of rockhead elevation.

Experiment	RMSE (m)	RMSRE	CP (%)
1	8.24	0.89	98
2	10.13	2.38	100
3	10.72	0.49	92
4	7.62	0.83	100
5	9.30	2.00	98
6	7.98	1.65	100
7	9.30	1.72	98
8	9.30	2.22	98
9	9.36	1.27	98
10	10.13	1.38	95
11	8.51	0.50	98
12	10.22	0.35	98
13	9.39	1.08	100
14	10.30	0.80	92
15	7.65	0.71	100
16	8.84	1.68	100
17	9.49	1.85	100
18	11.48	1.33	95
19	10.83	2.04	95
20	10.28	1.11	95
21	9.39	2.71	95
22	8.99	0.72	100
23	9.29	2.43	98
24	9.19	1.72	100
25	9.11	1.37	100
26	6.07	1.25	100
27	8.74	2.31	100
28	8.52	0.77	100
29	9.38	1.20	95
30	8.24	1.64	98
Average	9.22	1.47	98

Note: the last row summarizes the average value for 50 experiments. For brevity, the table only lists the results for 30 experiments.

5 Summary and conclusions

This study presented a multivariate adaptive regression spline (MARS) method to predict the elevations of geological interfaces based on limited borehole data. Borehole data from two sites in Singapore were used to evaluate the performance of the MARS method. The interfaces between the Kallang Formation (KF) and the Old Alluvium (OA) for the first site and the rockhead of the Bukit Timah Granite (BTG) for the second site were determined. The prediction accuracy of the MARS method was evaluated by a cross-validation procedure. By comparing the predicted surface of the geological interfaces with the bore-

hole data used for testing, it was found that the MARS method produced a reasonable prediction error (mean of root mean square error = 4.4 m) for the predicted elevations of the KF–OA interface. For the BTG rockhead elevation, the prediction error was higher than that of the first site because of the large variability of rockhead and the insufficient amount of data. The MARS method seems to have provided a reasonable prediction interval in the sense that the percentage of testing data covered by the 95% prediction interval was close to the confidence level, 95%. More importantly, the width of the prediction interval was consistent with the data density and geological complexity. In other words, the prediction interval was relatively wide at locations with sparse data and erratic geological conditions. It should be noted that for the considered prediction problem, the predicted surface of the geological interface was a surface representing the mean trend of the geological interfaces and did not run through all the known points of the geological interfaces.

Declaration of Competing Interest

The authors declare that they have no known competing financial interests or personal relationships that could have appeared to influence the work reported in this paper.

Acknowledgements

This research is supported by the Singapore Ministry of National Development and the National Research Foundation, Prime Minister's Office under the Land and Livability National Innovation Challenge (L2 NIC) Research Programme (Award No. L2NICCFP2-2015-1). Any opinions, findings, and conclusions or recommendations expressed in this material are those of the authors and do not reflect the views of the Singapore Ministry of National Development and National Research Foundation, Prime Minister's Office, Singapore.

Appendix A

The coordinates (x , y) and elevation (Ele) of the KF–OA interface and BTG rockhead used in this study are summarized in [Tables A1 and A2](#), respectively.

Table A1
Borehole data used for spatial predictions of Kallang Formation–Old Alluvium interface.

x (m)	y (m)	Ele (m)	x (m)	y (m)	Ele (m)	x (m)	y (m)	Ele (m)	x (m)	y (m)	Ele (m)
47.32	86.46	−12.07	273.52	149.04	−23.88	613.68	198.56	−22.68	903.21	385.26	−10.45
0.00	202.24	−13.41	142.94	371.57	−13.39	694.70	80.41	−25.14	1128.29	20.38	−17.37
1.67	218.44	−14.46	188.73	314.86	−15.68	613.18	246.01	−20.22	1118.58	48.81	−20.15
3.43	237.66	−21.41	230.73	262.54	−22.49	694.34	148.03	−24.41	932.17	368.23	−18.96
114.19	81.57	−1.42	181.06	351.78	−12.30	741.83	99.77	−25.82	1013.19	249.01	−21.66
5.42	264.16	−16.82	206.01	338.65	−15.24	612.26	325.97	−14.02	1114.63	81.21	−23.23
22.25	245.16	−17.43	290.83	204.92	−14.58	772.78	73.92	−16.58	1088.57	130.25	−16.01
83.59	147.82	−12.09	371.51	76.59	−12.70	693.05	246.64	−12.99	1135.64	55.91	−17.36

(continued on next page)

Appendix A1 (continued)

x (m)	y (m)	Ele (m)	x (m)	y (m)	Ele (m)	x (m)	y (m)	Ele (m)	x (m)	y (m)	Ele (m)
22.84	262.52	−14.45	333.65	163.78	−22.77	773.93	127.14	−25.90	1157.50	28.25	−19.52
153.10	78.95	−10.58	248.11	311.45	−17.37	820.95	90.43	−19.73	990.15	312.25	−11.67
23.79	308.95	−18.82	293.14	243.30	−14.15	835.85	66.36	−22.64	1127.80	85.23	−17.27
211.39	0.77	−23.46	247.62	339.82	−10.27	773.33	207.08	−13.69	1140.02	67.57	−17.41
59.43	258.56	−18.08	344.16	215.15	−15.29	686.43	355.50	−15.38	1080.85	173.64	−12.39
48.94	279.62	−18.36	291.64	326.47	−16.00	854.17	87.86	−26.97	1122.86	108.68	−23.33
145.77	122.12	−12.01	339.23	248.15	−25.21	895.00	59.99	−26.00	1128.89	133.57	−17.19
60.27	276.02	−18.20	373.53	200.27	−20.32	772.77	287.27	−15.37	1012.37	328.75	−15.70
64.91	268.52	−16.19	435.44	100.57	−15.95	855.59	171.99	−23.70	1086.22	210.53	−15.66
59.73	287.09	−18.20	493.96	10.54	−26.37	897.32	106.43	−21.12	1138.96	125.02	−17.09
136.55	160.86	−23.90	425.29	129.72	−18.86	934.66	48.33	−25.93	1147.81	111.52	−17.37
35.77	338.59	−13.20	413.88	164.34	−19.29	828.93	239.32	−21.89	1132.30	154.21	−17.14
206.60	56.96	−19.20	332.66	307.96	−13.48	940.11	76.22	−16.07	1005.84	365.50	−15.78
89.96	251.58	−17.99	378.20	255.38	−17.20	772.27	367.28	−16.69	1153.63	128.72	−20.48
43.05	345.37	−18.90	539.71	15.57	−16.81	868.86	221.20	−23.65	1136.68	175.72	−20.15
251.65	0.00	−13.65	408.68	242.38	−20.62	934.13	128.22	−15.75	1146.27	170.60	−13.04
88.29	290.05	−24.02	449.96	195.35	−19.94	977.16	64.28	−19.51	1091.75	289.37	−18.76
84.21	300.40	−15.06	372.43	339.35	−22.59	1005.54	17.87	−26.15	1154.79	195.01	−17.12
39.13	378.23	−18.91	414.69	307.30	−17.19	896.96	258.93	−25.34	1162.48	228.76	−14.17
42.20	386.48	−15.95	453.20	244.80	−19.47	867.71	308.71	−14.52	1084.73	364.83	−12.10
235.10	83.37	−12.48	569.73	55.21	−26.87	843.67	355.19	−9.25	1165.93	245.44	−11.18
114.63	284.58	−15.03	502.19	168.20	−22.67	940.30	199.84	−24.36	1157.55	268.97	−14.04
177.51	200.79	−20.24	452.87	284.81	−17.72	1048.19	22.52	−20.33	1169.12	265.65	−14.11
156.54	237.36	−17.68	493.14	245.10	−13.18	1015.04	80.76	−20.15	1177.17	297.87	−12.79
178.04	201.97	−20.38	551.77	147.60	−16.78	1054.41	57.65	−19.36	1187.70	285.22	−13.42
117.42	308.99	−17.95	552.76	147.57	−16.34	932.82	288.56	−22.29	1184.61	349.89	−13.50
163.80	282.55	−13.97	533.44	201.27	−22.09	1013.35	169.31	−11.90	1188.83	345.73	−14.16
213.21	202.83	−20.61	619.17	59.76	−23.48	965.99	255.36	−25.52	1188.97	383.81	−10.93
121.08	367.19	−14.94	452.39	344.02	−7.38	1103.68	27.75	−17.38	1212.63	390.58	−10.37
292.91	97.22	−12.65	532.73	285.30	−14.11	929.40	328.65	−25.38			
262.76	163.46	−21.68	658.95	91.06	−24.69	1114.60	31.09	−14.93			

Table A2

Borehole data used for spatial predictions of Bukit Timah granite rockhead.

x (m)	y (m)	Ele (m)	x (m)	y (m)	Ele (m)	x (m)	y (m)	Ele (m)	x (m)	y (m)	Ele (m)
12.64	332.04	−20.54	197.26	342.77	−27.82	318.34	328.43	−15.28	502.98	351.20	−17.22
51.89	345.53	−20.67	72.05	113.97	−7.50	207.92	125.23	−17.70	472.34	292.49	−8.70
44.30	321.94	−18.27	76.83	122.13	−1.25	166.65	48.80	−36.71	467.12	274.44	−18.16
42.49	294.36	−15.71	89.07	135.92	−7.88	201.73	101.37	−26.39	496.71	286.30	−31.79
79.67	348.69	−22.69	66.99	93.77	2.86	251.47	180.80	−6.41	386.77	84.93	−20.40
72.68	327.43	−16.39	178.69	293.49	−21.21	342.93	344.96	−14.59	475.54	242.67	−13.40
17.57	212.10	−23.16	66.24	84.54	2.52	314.20	289.21	−29.73	445.62	172.34	−31.76
49.58	261.27	−27.25	77.99	97.46	3.56	298.83	259.89	−28.74	505.88	271.33	−23.10
0.00	156.80	−14.74	66.14	72.01	1.68	197.19	32.66	−50.83	433.00	139.32	−11.88
113.38	349.11	−25.70	226.98	354.59	−25.30	227.03	77.87	−35.40	356.31	0.00	−25.77
100.81	324.14	−24.48	98.19	115.17	−10.00	256.75	127.75	−22.94	522.16	295.70	−19.08
94.29	295.06	−18.60	222.25	334.84	−21.29	282.08	165.72	−49.54	557.22	349.23	−18.80
25.93	145.83	−15.11	180.84	258.39	−9.78	220.82	48.85	−44.19	470.10	189.63	−16.26
37.69	158.75	−6.84	130.25	166.81	−10.22	304.36	178.25	−46.24	405.03	62.20	−15.58
132.10	321.75	−26.27	132.43	153.76	−16.47	266.30	83.35	−45.21	478.75	192.84	−21.40
49.44	171.66	−4.37	78.97	47.73	2.40	296.48	133.57	−43.62	505.85	230.56	−13.24
38.46	145.73	−12.11	176.48	221.20	−2.40	347.47	224.83	−29.00	436.20	89.49	−21.88
3.89	81.43	−12.58	133.22	127.59	−12.48	329.65	181.86	−12.40	459.42	129.22	−28.93
62.07	184.10	−5.60	262.12	356.49	−20.23	384.76	273.13	−11.60	525.37	245.87	−9.05
150.05	339.10	−29.17	162.78	174.16	−19.74	375.40	235.38	−21.38	412.31	23.84	−17.80
62.45	172.44	−5.07	133.45	116.98	−6.99	429.13	323.50	−26.15	448.74	89.40	−19.30
110.02	256.78	−28.28	217.73	258.03	−14.76	413.30	277.01	−18.59	506.04	171.96	−33.12
69.74	161.60	1.00	179.69	171.37	−3.40	332.86	132.04	−21.40	490.98	134.56	−28.09
158.30	317.28	−22.28	183.73	178.39	−6.22	320.60	109.56	−36.05	440.28	39.18	−15.18
86.74	185.26	−12.40	264.34	301.75	−11.03	422.02	288.41	−10.58	454.07	57.83	−23.55
52.16	120.96	2.55	296.01	357.19	−19.26	283.40	36.57	−32.71	443.39	18.01	−24.47

(continued on next page)

Appendix A2 (continued)

x (m)	y (m)	Ele (m)	x (m)	y (m)	Ele (m)	x (m)	y (m)	Ele (m)	x (m)	y (m)	Ele (m)
74.89	159.81	3.31	168.02	122.24	−6.53	314.37	86.10	−23.72	561.63	229.68	−22.29
40.31	95.52	3.36	288.28	333.65	−16.25	290.32	28.69	−24.40	486.03	92.70	−26.58
28.94	70.94	1.28	192.36	158.67	−14.48	379.48	185.07	−6.40	532.65	145.73	−34.50
87.12	173.61	−6.87	250.08	258.94	−16.25	304.50	49.85	−23.75	509.44	95.71	−39.50
76.15	147.67	0.79	214.05	172.14	−8.75	437.43	270.49	−18.31	491.96	53.94	−25.86
87.90	160.59	−5.74	170.59	84.78	−24.10	336.94	81.72	−22.40	536.34	96.78	−33.18
182.90	327.84	−28.31	141.22	17.72	−31.40	407.94	180.70	−22.40	539.55	46.95	−23.88
96.44	162.86	−22.97	229.51	174.58	−10.40	382.69	135.24	−18.18			

References

- Adoko, A. C., Jiao, Y. Y., Wu, L., Wang, H., & Wang, Z. H. (2013). Predicting tunnel convergence using multivariate adaptive regression spline and artificial neural network. *Tunnelling and Underground Space Technology*, 38, 368–376.
- Aswar, D. S., & Ullagaddi, P. B. (2017). An overview of 3-D geological modelling part II. Summary of major 3-d geological modelling methodologies. *International Journal of Latest Engineering and Management Research*, 2(11), 15–27.
- British Standard Committee (1999). BS 5930: 1999 Code of practice for site investigations. London: British Standards Institution.
- Burke, H., Ford, J., Hughes, L., Thorpe, S., & Lee, J. (2017). A 3D geological model of the superficial deposits in the Selby area (CR/17/112N) (Unpublished). *British Geological Survey*, 61.
- Cao, Z., & Wang, Y. (2012). Bayesian approach for probabilistic site characterization using cone penetration tests. *Journal of Geotechnical and Geoenvironmental Engineering*, 139(2), 267–276.
- Carroll, R., & Ruppert, D. (1988). Transformation and weighting in regression. New York, USA: Springer Science.
- Chang, L. Y. (2017). Exploring contributory factors to highway accidents: A nonparametric multivariate adaptive regression spline approach. *Journal of Transportation Safety & Security*, 9(4), 419–438.
- Ching, J., Wang, J. S., Juang, C. H., & Ku, C. S. (2015). Cone penetration test (CPT)-based stratigraphic profiling using the wavelet transform modulus maxima method. *Canadian Geotechnical Journal*, 52(12), 1993–2007.
- Dasaka, S. M., & Zhang, L. M. (2012). Spatial variability of in situ weathered soil. *Géotechnique*, 62(5), 375–384.
- Davidian, M., & Carroll, R. J. (1987). Variance function estimation. *Journal of the American Statistical Association*, 82(400), 1079–1091.
- Deng, Z. P., Li, D. Q., Qi, X. H., Cao, Z. J., & Phoon, K. K. (2017). Reliability evaluation of slope considering geological uncertainty and inherent variability of soil parameters. *Computers and Geotechnics*, 92, 121–131.
- Friedman, J. H. (1991). Multivariate adaptive regression splines. *Annals of Statistics*, 19(1), 1–67.
- Galecki, A., & Burzykowski, T. (2013). *Linear mixed-effects models using R: A step-by-step approach*. Springer Science & Business Media. <https://doi.org/10.1007/978-1-4614-3900-4>.
- Goh, A. T. C., Zhang, Y., Zhang, R., Zhang, W., & Xiao, Y. (2017). Evaluating stability of underground entry-type excavations using multivariate adaptive regression splines and logistic regression. *Tunnelling and Underground Space Technology*, 70, 148–154.
- Goh, A. T. C., Zhang, W., Zhang, Y., Xiao, Y., & Xiang, Y. (2018). Determination of earth pressure balance tunnel-related maximum surface settlement: A multivariate adaptive regression splines approach. *Bulletin of Engineering Geology and the Environment*, 77(2), 489–500.
- James, G., Witten, D., Hastie, T., & Tibshirani, R. (2013). *An introduction to statistical learning*. New York, USA: Springer.
- Hastie, T., Tibshirani, R., & Friedman, J. (2008). *The elements of statistical learning: Data mining, inference and prediction* (2nd ed.). New York, USA: Springer.
- Kisi, O., & Parmar, K. S. (2016). Application of least square support vector machine and multivariate adaptive regression spline models in long term prediction of river water pollution. *Journal of Hydrology*, 534, 104–112.
- Li, D. Q., Qi, X. H., Cao, Z. J., Tang, X. S., Phoon, K. K., & Zhou, C. B. (2016). Evaluating slope stability uncertainty using coupled Markov chain. *Computers and Geotechnics*, 73, 72–82.
- Li, J., Cai, Y., Li, X., & Zhang, L. (2019). Simulating realistic geological stratigraphy using direction-dependent coupled Markov chain model. *Computers and Geotechnics*, 115, 103147.
- Liu, L., Zhang, S., Cheng, Y. M., & Liang, L. (2019). Advanced reliability analysis of slopes in spatially variable soils using multivariate adaptive regression splines. *Geoscience Frontiers*, 10(2), 671–682.
- Mariethoz, G., & Caers, J. (2014). Multiple-point geostatistics: Stochastic modeling with training images. Chichester, UK: John Wiley & Sons.
- Milborrow, S. (2019a). Notes on the earth package. <http://www.milbo.org/doc/earth-notes.pdf>, 2019(11).
- Milborrow, S. (2019b). Variance models in earth. <http://www.milbo.org/doc/earth-varmod.pdf>, 2019(11).
- Pitts, J. (1984). A review of geology and engineering geology in Singapore. *Quarterly Journal of Engineering Geology and Hydrogeology*, 17(2), 93–101.
- Priya, B. D., & Dodagoudar, G. (2015). Spatial variability of soil-rock interface in Chennai using geophysical and geotechnical data. Geotechnical safety and risk V, 178. *International symposium on geotechnical safety and risk*, At Rotterdam, Netherlands.
- Qi, X. H., Li, D. Q., Phoon, K. K., Cao, Z. J., & Tang, X. S. (2016). Simulation of geologic uncertainty using coupled Markov chain. *Engineering Geology*, 207, 129–140.
- Qi, X. H., & Liu, H. X. (2019). An improved global zonation method for geotechnical parameters. *Engineering Geology*, 248, 185–196.
- Qi, X. H., Pan, X. H., Chiam, K., Lim, Y. S., & Lau, S. G. (2020). Comparative spatial predictions of the locations of soil-rock interface. *Engineering and Geology*, 272, 105651.
- Samui, P. (2012). Slope stability analysis using multivariate adaptive regression spline. *Metaheuristics in Water, Geotechnical and Transportation Engineering*, 14, 327–342.
- Samui, P., Kim, D., & Viswanathan, R. (2015). Spatial variability of rock depth using adaptive neuro-fuzzy inference system (ANFIS) and multivariate adaptive regression spline (MARS). *Environmental Earth Sciences*, 73(8), 4265–4272.
- Sharma, J. S., Chu, J., & Zhao, J. (1999). Geological and geotechnical features of Singapore: An overview. *Tunnelling and Underground Space Technology*, 14(4), 419–431.
- Shirlaw, J. N., Hencher, S. R., & Zhao, J. (2000). Design and construction issues for excavation and tunnelling in some tropically weathered rocks and soils. *ISRM international symposium*. International Society for Rock Mechanics and Rock Engineering.
- Wang, X., Wang, H., Liang, R. Y., Zhu, H., & Di, H. (2018). A hidden Markov random field model based approach for probabilistic site characterization using multiple cone penetration test data. *Structural Safety*, 70, 128–138.
- Wang, Y., & Zhao, T. (2016). Interpretation of soil property profile from limited measurement data: A compressive sampling perspective. *Canadian Geotechnical Journal*, 53(9), 1547–1559.
- Wang, Y., & Zhao, T. (2017). Statistical interpretation of soil property profiles from sparse data using Bayesian compressive sampling. *Géotechnique*, 67(6), 523–536.
- Wang, H., Wellmann, J. F., Li, Z., Wang, X., & Liang, R. Y. (2017). A segmentation approach for stochastic geological modeling using hidden Markov random fields. *Mathematical Geosciences*, 49(2), 145–177.
- Wang, Y., Akeju, O. V., & Zhao, T. (2017). Interpolation of spatially varying but sparsely measured geo-data: A comparative study. *Engineering Geology*, 231, 200–217.
- Wang, L., Wu, C., Gu, X., Liu, H., Mei, G., & Zhang, W. (2020). Probabilistic stability analysis of earth dam slope under transient seepage using multivariate adaptive regression splines. *Bulletin of*

- Engineering Geology and the Environment*. <https://doi.org/10.1007/s10064-020-01730-0> (in press).
- Woon, L. K., & Zhou, Y. (2009). *Geology of Singapore*. Singapore: Defence Science and Technology Agency.
- Zhao, T., Hu, Y., & Wang, Y. (2018a). Statistical interpretation of spatially varying 2D geo-data from sparse measurements using Bayesian compressive sampling. *Engineering Geology*, 246, 162–175.
- Zhao, T., Montoya-Noguera, S., Phoon, K. K., & Wang, Y. (2018b). Interpolating spatially varying soil property values from sparse data for facilitating characteristic value selection. *Canadian Geotechnical Journal*, 55(2), 171–181.
- Zhang, W., & Goh, A. T. (2013). Multivariate adaptive regression splines for analysis of geotechnical engineering systems. *Computers and Geotechnics*, 48, 82–95.
- Zhang, W., & Goh, A. T. (2016). Multivariate adaptive regression splines and neural network models for prediction of pile drivability. *Geoscience Frontiers*, 7(1), 45–52.
- Zhang, W., & Goh, A. T. C. (2017). Reliability assessment of ultimate limit state of twin caverns. *Geomechanics and Geoengineering*, 12(1), 48–59.
- Zhang, W., Goh, A. T. C., Zhang, Y., Chen, Y. M., & Xiao, Y. (2015). Assessment of soil liquefaction based on capacity energy concept and multivariate adaptive regression splines. *Engineering Geology*, 188, 29–37.
- Zhang, W., Zhang, Y., & Goh, A. T. C. (2017). Multivariate adaptive regression splines for inverse analysis of soil and wall properties in braced excavation. *Tunnelling and Underground Space Technology*, 64, 24–33.
- Zhang, W., Zhang, R., & Goh, A. T. C. (2018). Multivariate adaptive regression splines approach to estimate lateral wall deflection profiles caused by braced excavations in clays. *Geotechnical and Geological Engineering*, 36(2), 1349–1363.
- Zhang, W., Zhang, R., Wang, W., Zhang, F., & Goh, A. T. C. (2019a). A multivariate adaptive regression splines model for determining horizontal wall deflection envelope for braced excavations in clays. *Tunnelling and Underground Space Technology*, 84, 461–471.
- Zhang, W., Zhang, R., Wu, C., Goh, A. T. C., Lacasse, S., Liu, Z., & Liu, H. (2019b). State-of-the-art review of soft computing applications in underground excavations. *Geoscience Frontiers*. <https://doi.org/10.1016/j.gsf.2019.12.003> (in press).
- Zhang, W., Wu, C., Li, Y., Wang, L., & Samui, P. (2019c). Assessment of pile drivability using random forest regression and multivariate adaptive regression splines. *Georisk: Assessment and Management of Risk for Engineered Systems and Geohazards*. <https://doi.org/10.1080/17499518.2019.1674340> (in press).
- Zhang, W. G., Li, H. R., Wu, C. Z., Li, Y. Q., Liu, Z. Q., & Liu, H. L. (2020). Soft computing approach for prediction of surface settlement induced by earth pressure balance shield tunneling. *Underground Space*. <https://doi.org/10.1016/j.undsp.2019.12.003> (in press).
- Zhao, J., Broms, B., Zhou, Y., & Choa, V. (1994). A study of the weathering of the Bukit Timah granite part A: Review, field observations and geophysical survey. *Bulletin of the International Association of Engineering Geology-Bulletin de l'Association Internationale de Géologie de l'Ingénieur*, 49(1), 97–106.